GENOME EDITING

Dynamics of CRISPR-Cas9 genome interrogation in living cells

Spencer C. Knight,[1] Liangqi Xie,[2] Wulan Deng,[3,4] Benjamin Guglielmi,[2] Lea B. Witkowsky,[2] Lana Bosanac,[2] Elisa T. Zhang,[2] Mohamed El Beheiry,[5] Jean-Baptiste Masson,[3] Maxime Dahan,[4,5] Zhe Liu,[3,4]* Jennifer A. Doudna,[1,2,6,7,8]* Robert Tjian[2,3,4,6,9]*

The RNA-guided CRISPR-associated protein Cas9 is used for genome editing, transcriptional modulation, and live-cell imaging. Cas9-guide RNA complexes recognize and cleave double-stranded DNA sequences on the basis of 20-nucleotide RNA-DNA complementarity, but the mechanism of target searching in mammalian cells is unknown. Here, we use single-particle tracking to visualize diffusion and chromatin binding of Cas9 in living cells. We show that three-dimensional diffusion dominates Cas9 searching in vivo, and off-target binding events are, on average, short-lived (<1 second). Searching is dependent on the local chromatin environment, with less sampling and slower movement within heterochromatin. These results reveal how the bacterial Cas9 protein interrogates mammalian genomes and navigates eukaryotic chromatin structure.

The RNA-guided endonuclease Cas9 uses RNA-DNA complementarity to target and cleave double-stranded DNA upstream of a protospacer-adjacent motif (PAM) (*1*, *2*). Cas9 can be programmed with a single-guide RNA (sgRNA) to cleave specific DNA sequences within eukaryotic cells, which facilitates its use as a tool for genome engineering (*3*–*5*). Biochemical and genome occupancy studies have established the PAM and adjacent ~5 to 8 base pairs (the "seed" region) of the DNA target site as the basis for Cas9 DNA interrogation and off-target activity (*1*, *6*–*13*). Nonetheless, how Cas9 explores large eukaryotic genomes and identifies targets within the context of chromatin remains largely unknown. In particular, the in vivo kinetics of on- versus off-target binding and Cas9 dependence on the chromatin environment have not yet been examined in living eukaryotic cells.

To investigate the live-cell dynamics of Cas9 target searching, we tracked single, fluorescently labeled, catalytically inactive *Streptococcus pyogenes* Cas9 (dCas9) molecules to determine their diffusion and chromatin binding properties in live mouse cell nuclei (*14*). dCas9 was fused at its C terminus with a HaloTag domain and stably integrated into the genome of NIH 3T3 cells under an inducible, tetracycline response element (TRE)–tight promoter (Fig. 1A and figs. S1 to S3) (*15*). Guide RNAs were transiently expressed from a blue fluorescent protein (BFP) reporter plasmid. Covalent linkage of a cell-permeable, fluorescent HaloTag ligand (JF549) allowed for visualization of single Cas9-HaloTag molecules under leaky expression (Fig. 1, A and B, and fig. S4) (*16*).

To study dCas9-HaloTag binding dynamics at endogenous genomic loci, we transfected cells with a guide RNA targeted to short interspersed nuclear elements (SINEs) of the B2 type. The B2 elements are repeated ~350,000 times throughout the mouse genome, often in intragenic regions, with a single element per insertion site (*17*, *18*). We reasoned that the abundance of these loci would shift the global equilibrium of Cas9-HaloTag binding and allow us to observe otherwise rare target-binding events. Two-photon fluorescence correlation spectroscopy (FCS) experiments revealed a substantial reduction in global dCas9-HaloTag mobility for B2 sgRNA-transfected cells relative to apo (no sgRNA) protein (Fig. 1C). Both apo and B2-loaded dCas9-HaloTag displayed biphasic kinetic behavior in our FCS measurements, which reflected slowly and rapidly moving populations for both conditions. The magnitude of the slow diffusion coefficient was reduced by >90% in the presence of B2 sgRNA relative to the apo protein (fig. S5).

We conducted two-dimensional (2D) tracking experiments at short (10-ms) exposure times in cells transfected with a plasmid encoding either B2 or a phage-derived "nonsense" guide bearing minimal homology to the 3T3 genome (figs. S6 to S8). A nonsense sgRNA has the potential to direct Cas9 off-target interactions through millions of PAMs and short seed sequences within the genome and thus serves as a proxy for a Cas9 protein in the process of searching (*1*, *6*). The

[1]Department of Chemistry, University of California, Berkeley, CA, USA. [2]Department of Molecular and Cell Biology, University of California, Berkeley, CA, USA. [3]Janelia Research Campus, Howard Hughes Medical Institute, Ashburn, VA, USA. [4]Transcriptional Imaging Consortium, Janelia Research Campus, Howard Hughes Medical Institute, Ashburn, VA, USA. [5]Laboratoire Physico-Chimie Curie, Institut Curie, Centre National de la Recherche Scientifique UMR 168, Paris, France. [6]Howard Hughes Medical Institute, Department of Molecular and Cell Biology, University of California, Berkeley, CA, USA. [7]Physical Biosciences Division, Lawrence Berkeley National Laboratory, Berkeley, CA, USA. [8]Innovative Genomics Initiative, University of California, Berkeley, CA, USA. [9]Li Ka Shing Biomedical and Health Sciences Center, University of California, Berkeley, CA, USA.
*Corresponding author. E-mail: liuz11@janelia.hhmi.org (Z.L.); doudna@berkeley.edu (J.A.D.); jmlim@berkeley.edu (R.T.)

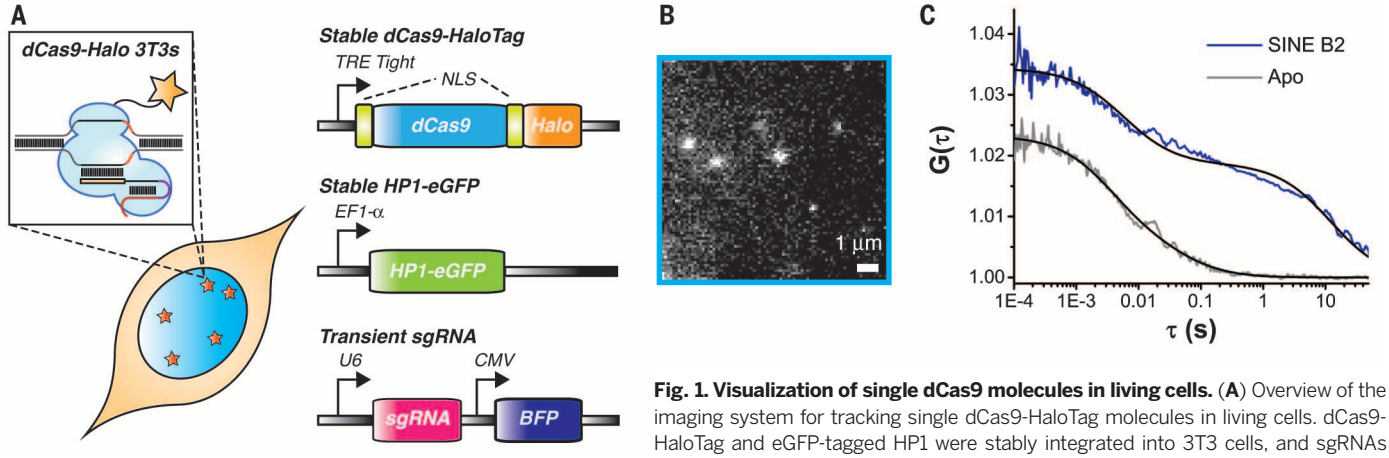

Fig. 1. Visualization of single dCas9 molecules in living cells. (**A**) Overview of the imaging system for tracking single dCas9-HaloTag molecules in living cells. dCas9-HaloTag and eGFP-tagged HP1 were stably integrated into 3T3 cells, and sgRNAs were transiently transfected. (**B**) 2D single-molecule visualization of dCas9-HaloTag molecules within live 3T3 nuclei during a 10-ms exposure. (**C**) Two-photon FCS correlation curves and mathematical fits for dCas9-HaloTag in the absence of sgRNA (apo, gray) or loaded with cognate SINE B2 sgRNA (blue). Fluorescence correlation was measured within diffraction-limited volumes over time at random locations within cell nuclei (N = 11 cells for each condition).

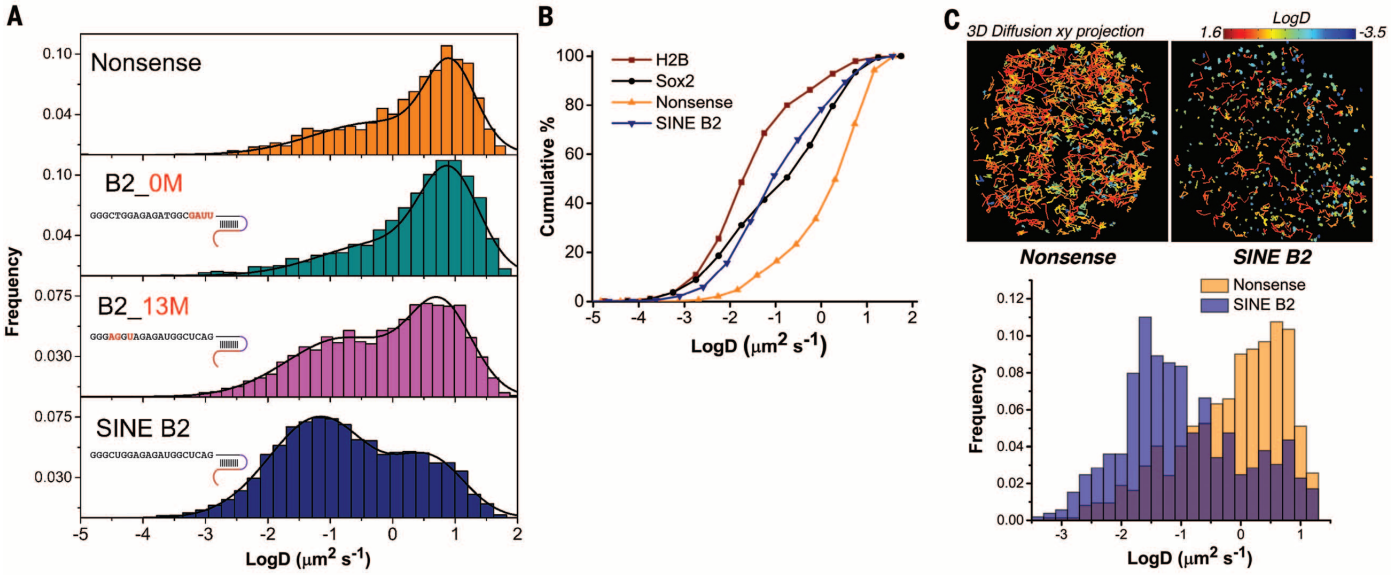

Fig. 2. Cas9 exploration is dominated by 3D diffusion during the search for target sites in vivo. (**A**) Normalized histograms and two-component Gaussian fits illustrating the log diffusion coefficient distributions for dCas9-HaloTag with different sgRNAs ($N \geq 12$ cells for each condition). For reference, chromatin-bound H2B molecules can be fitted with a single Gaussian with log$D \approx 0.1$ $\mu m^2 \cdot s^{-1}$. (**B**) Cumulative distribution plots quantifying the log diffusion coefficient for SINE B2 or nonsense-loaded dCas9-HaloTag relative to histone H2B or Sox2. (**C**) (Top) 2D projections of single-particle trajectories obtained from 3D imaging using a multifocus microscope. (Bottom) Histograms showing the log$D$ distribution of trajectories. The trajectories are color-coded according to diffusion coefficient. The 3D movies were collected at an exposure time of 30 ms, and diffusion coefficients were extracted directly from the mean square displacements of the 3D trajectories (*28*) ($N = 2$ cells for each condition).

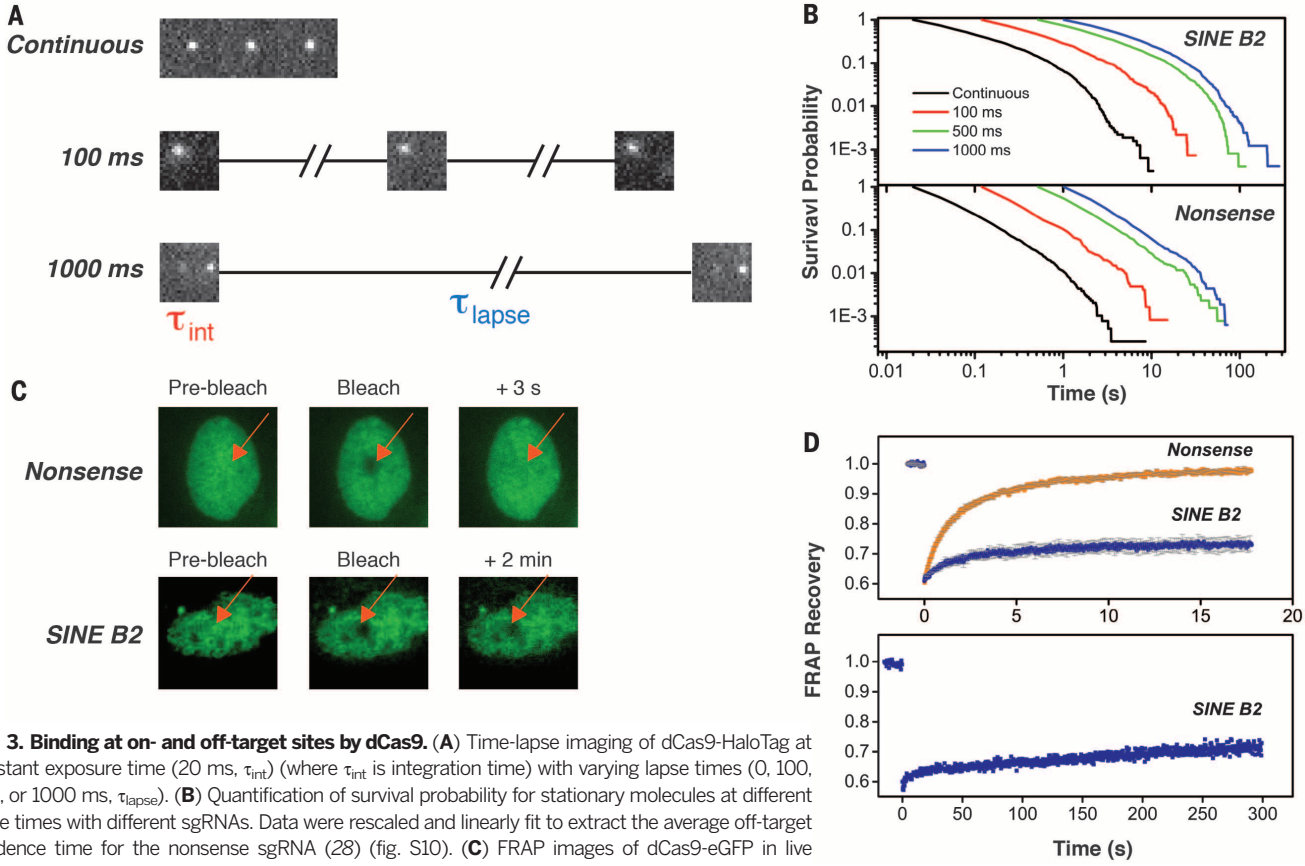

Fig. 3. Binding at on- and off-target sites by dCas9. (**A**) Time-lapse imaging of dCas9-HaloTag at constant exposure time (20 ms, τ_{int}) (where τ_{int} is integration time) with varying lapse times (0, 100, 500, or 1000 ms, τ_{lapse}). (**B**) Quantification of survival probability for stationary molecules at different lapse times with different sgRNAs. Data were rescaled and linearly fit to extract the average off-target residence time for the nonsense sgRNA (*28*) (fig. S10). (**C**) FRAP images of dCas9-eGFP in live mouse cells with either nonsense (top) or SINE B2 (bottom) sgRNA. (**D**) Quantification of FRAP images for dCas9-eGFP using different sgRNAs ($N = 17$ cells for each condition).

resulting log diffusion coefficient histograms showed a large fraction of highly immobile ($D < 0.1\ \mu m^2 \cdot s^{-1}$) Cas9 molecules for B2 sgRNA relative to nonsense sgRNA or no-guide controls, consistent with more chromatin binding for the B2-loaded Cas9 (Fig. 2A and fig. S9). In similar experiments, a B2 guide with mismatches proximal to the target PAM gave rise to Cas9 diffusion histograms similar to those of the nonsense guide; in contrast, a B2 guide with homology mismatches distal to the target PAM gave rise to a distribution more similar to the cognate B2 guide (B2_0M and B2_13M, respectively) (Fig. 2A and fig. S6). These observations are consistent with the noted role of the seed region in driving Cas9's RNA-guided interaction with DNA (*6*, *10*, *11*).

Compared with a binding-dominant protein (e.g., H2B) or a protein that demonstrates a mixture of binding and diffusion (e.g., Sox2), both the nonsense-loaded and apo Cas9 showed considerably more apparent 3D diffusion in cell nuclei (Fig. 2B, fig. S9, and movies S1 to S4). In addition, 3D multifocus tracking experiments with the nonsense guide showed that Cas9–guide RNA complexes use diffusion-dominated target searching throughout the entirety of the cell nucleus (Fig. 2C and movie S5) (*19*). These results underscore the dominance of 3D diffusion over binding during DNA interrogation by Cas9 and demonstrate an in vivo target search mechanism similar to what has been observed in vitro (*6*).

To determine the relative kinetics of on- versus off-target binding, we measured in vivo residence times of dCas9-HaloTag molecules bound to chromatin. We performed time-lapse experiments at a constant exposure time (20 ms, τ_{int}) while varying the lapse time τ_{lapse} between successive frames (Fig. 3A, movies S6 to S9). From these movies, we plotted the probability that a dCas9-HaloTag molecule would remain stationary as a function of time (survival probability) (Fig. 3B). Rescaling and concatenation of these plots allowed us to extract an average off-target residence time of 0.75 ± 0.1 s for Cas9 containing a nonsense guide (τ_{ns}) (fig. S10) (*20*, *21*). We note that a small fraction of the binding events in our concatenated plot were longer than 10 s, which might be attributed to rare genomic sequences with higher homology to the nonsense guide (fig. S10) (*6*, *22*). We also measured the binding of nonsense-loaded protein in dCas9-eGFP stable cell lines using fluorescence recovery after photobleaching (FRAP), a bulk technique for assessing protein mobility based on exchange between bleached and unbleached molecules within a region of interest. We observed nearly full recovery within 10 s, which indicated mostly transient (milliseconds to seconds) chromatin interactions intermixed with diffusion (Fig. 3, C and D) (*23*).

Although nonsense guide–loaded dCas9-eGFP recovered rapidly after photobleaching in our FRAP curves, the B2 guide–loaded protein resulted in a large immobile fraction even when measured out to 5 min (Fig. 3, C and D, and movies S10 to S12). Similarly, survival probability plots of B2 guide–loaded Cas9 showed substantially longer residence times compared with those with the nonsense guide (Fig. 3B). These data suggest that Cas9 binding at bona fide targets (τ_s) could be considerably longer (i.e., minutes or more) in vivo relative to short-lived (milliseconds to seconds) binding typical of PAMs and very short seed sequences (τ_{ns}) (*6*). We refrain from more precisely estimating τ_s here because of (i) a likely mixture of off-target and on-target binding in the immobile fraction, (ii) imaging limitations due to photobleaching in our single-molecule measurements (curved tails) (Fig. 3B), and (iii) known complications with extracting residence times from FRAP data (*24*).

The ability of Cas9 to target heterochromatic regions (HRs) is important for its application to genome editing. To study Cas9 behavior in HRs, we performed tracking experiments in cells with eGFP-labeled heterochromatin protein 1 (HP1) (fig. S11) (*25*–*28*). dCas9-HaloTag molecules with nonsense sgRNA were stochastically excited and tracked in live-cell nuclei, and the trajectories were overlaid onto HP1-labeled nuclear images to visualize searching with respect to heterochromatin. The resulting composite image shows marked depletion of tracks within HRs (30 ± 9% track density reduction) (fig. S11). Diffusion analysis of tracks within HRs revealed that dCas9 diffusion is moderately slower in these regions (Fig. 4A and fig. S12) (*29*). We also performed jumping angle analysis on three-point sliding windows of our Cas9 trajectories to monitor the anisotropy of searching in HRs (*28*, *30*). The resulting angle distributions revealed a slight bias toward reverse (180°) angles, which suggested more compact exploration and a tendency of Cas9 to return to its starting point while interrogating heterochromatin (Fig. 4B and fig. S13). Together, these results show that Cas9 search efficiency is reduced, but not eliminated, in HRs.

To test whether dCas9 can bind to target sites in heterochromatin, we transfected cells expressing dCas9-HaloTag with a plasmid encoding a sgRNA targeted to pericentromeric DNA sequences within heterochromatin. We observed distinct puncta within HRs of fixed cells colocalized with dense Hoechst staining, consistent with successful dCas9 targeting to pericentromeres (Fig. 4C). This result strongly suggests that Cas9 is able to bypass chromatin obstacles and faithfully engage with HR target sites despite reduced sampling efficiency within these regions.

Our data provide a direct visualization of DNA interrogation by Cas9 in mammalian cells. The target search mechanism involves rapid three-dimensional diffusion of Cas9 around the nucleus, with occasional forays into heterochromatic regions. Our imaging approach complements chromatin immunoprecipitation experiments by capturing many of the more transient interactions with DNA that predominate as Cas9 scans vast mammalian genomes in search of its target site. Overall, our results provide a quantitative understanding of

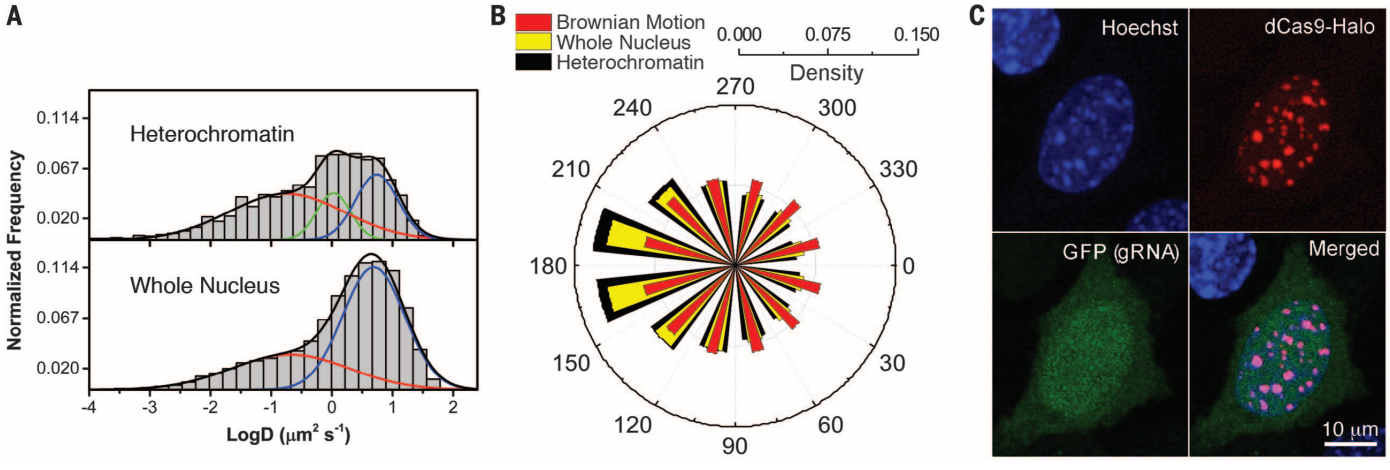

Fig. 4. Cas9 search efficiency is reduced, but not eliminated, in heterochromatic regions. (**A**) Log diffusion coefficient histograms and Gaussian fits for dCas9-HaloTag in HRs versus the entire cell nucleus (N = 11 cells). (**B**) Jumping angle analysis of diffusion anisotropy within HRs relative to the entire cell nucleus (N = 5 cells). (**C**) Epi-fluorescence image illustrating puncta formation in cells transfected with pericentromere-targeted sgRNA. Cells were fixed and costained with Hoechst 33258 for orthogonal labeling of pericentromeres.

Cas9 dynamics in living cells and offer insight into how Cas9 navigates hierarchical organization of DNA within a eukaryotic nucleus.

REFERENCES AND NOTES

1. M. Jinek *et al.*, *Science* **337**, 816–821 (2012).
2. G. Gasiunas, R. Barrangou, P. Horvath, V. Siksnys, *Proc. Natl. Acad. Sci. U.S.A.* **109**, E2579–E2586 (2012).
3. P. D. Hsu, E. S. Lander, F. Zhang, *Cell* **157**, 1262–1278 (2014).
4. J. A. Doudna, E. Charpentier, *Science* **346**, 1258096 (2014).
5. R. M. Terns, M. P. Terns, *Trends Genet.* **30**, 111–118 (2014).
6. S. H. Sternberg, S. Redding, M. Jinek, E. C. Greene, J. A. Doudna, *Nature* **507**, 62–67 (2014).
7. M. Jinek *et al.*, *Science* **343**, 1247997 (2014).
8. H. Nishimasu *et al.*, *Cell* **156**, 935–949 (2014).
9. C. Anders, O. Niewoehner, A. Duerst, M. Jinek, *Nature* **513**, 569–573 (2014).
10. X. Wu *et al.*, *Nat. Biotechnol.* **32**, 670–676 (2014).
11. C. Kuscu, S. Arslan, R. Singh, J. Thorpe, M. Adli, *Nat. Biotechnol.* **32**, 677–683 (2014).
12. P. D. Hsu *et al.*, *Nat. Biotechnol.* **31**, 827–832 (2013).
13. V. Pattanayak *et al.*, *Nat. Biotechnol.* **31**, 839–843 (2013).
14. B. Chen *et al.*, *Cell* **155**, 1479–1491 (2013).
15. G. V. Los *et al.*, *ACS Chem. Biol.* **3**, 373–382 (2008).
16. J. B. Grimm *et al.*, *Nat. Methods* **12**, 244–250, 3, 250 (2015).
17. J. Jurka, O. Kohany, A. Pavlicek, V. V. Kapitonov, M. V. Jurka, *Cytogenet. Genome Res.* **110**, 117–123 (2005).
18. C. A. Espinoza, J. A. Goodrich, J. F. Kugel, *RNA* **13**, 583–596 (2007).
19. S. Abrahamsson *et al.*, *Nat. Methods* **10**, 60–63 (2013).
20. J. C. M. Gebhardt *et al.*, *Nat. Methods* **10**, 421–426 (2013).
21. D. Normanno *et al.*, *Nat. Commun.* **6**, 7357 (2015).
22. M. D. Szczelkun *et al.*, *Proc. Natl. Acad. Sci. U.S.A.* **111**, 9798–9803 (2014).
23. B. L. Sprague, R. L. Pego, D. A. Stavreva, J. G. McNally, *Biophys. J.* **86**, 3473–3495 (2004).
24. F. Mueller, D. Mazza, T. J. Stasevich, J. G. McNally, *Curr. Opin. Cell Biol.* **22**, 403–411 (2010).
25. J. C. Eissenberg, S. C. R. Elgin, *Curr. Opin. Genet. Dev.* **10**, 204–210 (2000).
26. Z. Liu *et al.*, *eLife* **3**, e04236 (2014).
27. S. Manley *et al.*, *Nat. Methods* **5**, 155–157 (2008).
28. Materials and Methods are available as supplementary materials on *Science* Online.
29. M. El Beheiry, M. Dahan, J. B. Masson, *Nat. Methods* **12**, 594–595 (2015).
30. I. Izeddin *et al.*, *eLife* **3**, e02230 (2014).

ACKNOWLEDGMENTS

We thank L. Lavis for generously providing HaloTag ligands for imaging experiments; J. Macklin for expert assistance with FCS experiments; and X. Darzacq, R. Singer, J. Cate, and members of the Doudna and Tjian labs for helpful discussions and critical reading of the manuscript. S.C.K. acknowledges support from the Janelia Visitor Program, S.C.K. and E.T.Z. acknowledge support from the National Science Foundation Graduate Research Fellowship Program, W.D. acknowledges support from the Helen Hay Whitney Foundation, and Z.L. acknowledges support from the Janelia Fellow Program. Funding was provided by the National Science Foundation (MCB-1244557 to J.A.D.) and the California Institute for Regenerative Medicine (CIRM, RB4-06016 to R.T.). J.A.D. and R.T. are Investigators of the Howard Hughes Medical Institute. This work was performed in part at the University of California Berkeley Cancer Research Laboratory Molecular Imaging Center, supported by the Gordon and Betty Moore Foundation. J.A.D. is a co-founder of Caribou Biosciences, Inc., Editas Medicine and Intellia Therapeutics.

SUPPLEMENTARY MATERIALS

www.sciencemag.org/content/350/6262/823/suppl/DC1
Materials and Methods
Table S1
Figs. S1 to S13
Captions for Movies S1 to S12
References (*31*–*38*)
Movies S1 to S12

27 May 2015; accepted 7 October 2015
10.1126/science.aac6572

ANTIVIRAL IMMUNITY

Nlrp6 regulates intestinal antiviral innate immunity

Penghua Wang,[1,6]* Shu Zhu,[2]* Long Yang,[1,6] Shuang Cui,[1] Wen Pan,[3] Ruaidhri Jackson,[2] Yunjiang Zheng,[2] Anthony Rongvaux,[2] Qiangming Sun,[1]† Guang Yang,[1]‡ Shandian Gao,[1] Rongtuan Lin,[4] Fuping You,[1] Richard Flavell,[2,5]§|| Erol Fikrig[1,5]§||

The nucleotide-binding oligomerization domain–like receptor (Nlrp) 6 maintains gut microbiota homeostasis and regulates antibacterial immunity. We now report a role for Nlrp6 in the control of enteric virus infection. *Nlrp6*$^{-/-}$ and control mice systemically challenged with encephalomyocarditis virus had similar mortality; however, the gastrointestinal tract of *Nlrp6*$^{-/-}$ mice exhibited increased viral loads. *Nlrp6*$^{-/-}$ mice orally infected with encephalomyocarditis virus had increased mortality and viremia compared with controls. Similar results were observed with murine norovirus 1. Nlrp6 bound viral RNA via the RNA helicase Dhx15 and interacted with mitochondrial antiviral signaling protein to induce type I/III interferons (IFNs) and IFN-stimulated genes (ISGs). These data demonstrate that Nlrp6 functions with Dhx15 as a viral RNA sensor to induce ISGs, and this effect is especially important in the intestinal tract.

Nucleotide oligomerization domain (NOD)–like receptors (NLRs) play a central role in the immune response to diverse microorganisms and react to environmental insults and cellular danger signals (*1*, *2*). Some NLRs contribute to antiviral immunity. NOD2 recognizes single-stranded RNA (ssRNA) viruses to induce type I interferons (IFNs) via mitochondrial antiviral-signaling protein (MAVS) (*3*), and the NLRP3 inflammasome is crucial for the control of diverse viral infections in vivo (*4*–*7*). Several NLRs, on the other hand, dampen antiviral immune responses. NLRX1 and NLRC5 negatively regulate type I IFNs and nuclear factor κB (NF-κB) signaling via distinct molecular mechanisms (*8*–*12*); NLRC3 attenuates Toll-like receptor signaling and the stimulator of interferon genes (STING)–mediated anti-DNA virus immune signaling (*13*, *14*). A role for Nlrp6 in the regulation of antibacterial immune responses has recently been documented (*15*–*18*); however, whether Nlrp6 regulates viral infection has not yet been elucidated.

Nlrp6 exhibits a tissue- and cell-type–specific pattern of expression, with the highest level in intestinal epithelial cells (IECs) (*15*) (figs. S1 and S2). We therefore determined whether Nlrp6 plays a prominent role in inhibiting enteric virus infection at the intestinal interface. We used a (+) ssRNA virus, encephalomyocarditis virus (EMCV), which is transmitted via the fecal-oral route in nature. We infected both wild-type (WT) and *Nlrp6*$^{-/-}$ mice with EMCV systemically via intraperitoneal injection and noted that the survival curve of *Nlrp6*$^{-/-}$ mice was similar to that of WT animals (Fig. 1A). Viral dissemination was also the same in the blood, brains, and hearts of *Nlrp6*$^{-/-}$ and WT mice. The intestinal viral burden of *Nlrp6*$^{-/-}$ mice was, however, higher than that of WT animals (Fig. 1B)—suggesting that Nlrp6 plays an important role in limiting EMCV replication at this location. In support of this, *Nlrp6* mRNA expression was much higher in the intestines than other tissues after EMCV infection (Fig. 1C). We therefore reasoned that Nlrp6 prevents systemic infection and mortality when EMCV is delivered orally to its principal site of infection—the intestine. Indeed, *Nlrp6*$^{-/-}$ mice were more susceptible to oral infection with EMCV than WT animals (Fig. 1D and Fig. 3E).

Alterations in microbiota and inflammasome activation are two potential processes that may influence the ability of *Nlrp6*$^{-/-}$ mice to control intestinal EMCV infection. The intestinal microbial ecology of *Nlrp6*$^{-/-}$ mice is different from that of WT mice (*15*), which could affect antiviral immunity. We therefore cohoused mice for 4 weeks before EMCV infection, which we previously showed was sufficient to equilibrate the microbiota between WT and *Nlrp6*$^{-/-}$ mice. WT and *Nlrp6*$^{-/-}$ mice had similar levels of *TM7* and *Prevotellacae* bacteria (*15*) after cohousing (fig. S3A), indicating stabilization of the microbiota. *Nlrp6*$^{-/-}$ mice, however, died of EMCV infection more rapidly than WT and cohoused WT animals (Fig. 1D), and viremia was ~10-fold higher in *Nlrp6*$^{-/-}$ than WT animals (Fig. 1E). When inoculated systemically

[1]Section of Infectious Diseases, Yale University School of Medicine, 300 Cedar Street, New Haven, CT 06510, USA. [2]Department of Immunobiology, Yale University School of Medicine, 300 Cedar Street, New Haven, CT 06510, USA. [3]Department of Genetics, Yale University School of Medicine, 300 Cedar Street, New Haven, CT 06510, USA. [4]Lady Davis Institute, Department of Medicine, McGill University, Montreal, Quebec, Canada. [5]Howard Hughes Medical Institute, Chevy Chase, MD 20815-6789, USA. [6]Department of Microbiology and Immunology, New York Medical College, Valhalla, NY 10595, USA.
*These authors contributed equally to this work. †Present address: Institute of Medical Biology, Chinese Academy of Medical Sciences, and Peking Union Medical College, Kunming, People's Republic of China. ‡Present address: Department of Parasitology, School of Medicine, Jinan University, Guangzhou, China. §The laboratories of these authors contributed equally to this work. **||Corresponding author. E-mail: richard.flavell@yale.edu (R.F.); erol.fikrig@yale.edu (E.F.)**

Dynamics of CRISPR-Cas9 genome interrogation in living cells

Spencer C. Knight *et al.*

Science **350**, 823 (2015);
DOI: 10.1126/science.aac6572